# Numerical prediction of loudness metrics for N-waves and shaped sonic booms in kinematic turbulence

Alexander N. Carr,[1] Joel B. Lonzaga,[2] and Steven A. E. Miller[1]
[1] *Department of Mechanical and Aerospace Engineering, University of Florida, Gainesville, Florida 32611, United States of America*
[2] *Structural Acoustics Branch, NASA Langley Research Center, Hampton, Virginia, 23665, United States of America*

(Dated: 1 June 2022)

The effects of a kinematic field of velocity fluctuations on the loudness metrics of two waveforms are examined with a three-dimensional one-way propagation solver. The waveforms consist of an N-wave and a simulated low boom from NASA's X-59 QueSST aircraft. The kinematic turbulence is generated using a von Kármán composite spectrum, which is dependent on a root-mean-square (rms) velocity and outer scale of the turbulence. A length scale is proposed to account for the effect of the rms velocity and integral scale on the focusing and defocusing of the sonic boom waveform. The probability density function of the location of the first caustic attains a maximum value when the propagation distance is equal to the proposed length scale. Simulation results indicate that for small values of the nondimensional propagation distance, the standard deviation of the loudness metrics increases linearly. The loudness metrics follow a normal distribution within a given range of the nondimensional propagation distance. Results indicate the potential to parameterize the loudness metric distributions by the rms velocity and integral length scale.
 [https://doi.org(DOI number)]

[XYZ] Pages: 1–15

## I. INTRODUCTION

Sonic boom waveforms measured at ground level exhibit variability that is not consistent with macroscale atmospheric effects[1,2] such as refraction due to atmospheric stratification as well as absorption from molecular relaxation and thermoviscous dissipation. Presently, this variability is understood to be an effect of the interaction of the sonic boom with atmospheric turbulence.[1] Turbulence in the atmospheric boundary layer (ABL) alters the waveform due to scattering, diffraction, and refraction effects.[3] Early computational works on sonic boom propagation were focused on predicting the macroscale atmospheric effects and neglected the effects of turbulence.[4–7] However, recent computational[8–10] and experimental[11,12] investigations have examined the effects of turbulence on sonic boom waveforms or spark generated N-waves. These investigations have provided insight into the effects of turbulence on the rise time and overpressure of N-waves.

Questions remain regarding the impact of turbulence root-mean-square (rms) velocity and length scales on the loudness metrics. Specifically, do the statistical moments, i.e., mean and variance, of the loudness metrics show similarity when propagating through fields of different rms velocity and length scale, and can the metrics be approximated by a known probability distribution? Knowledge of the distribution of loudness metrics in turbulence is critical to predicting the annoyance of new shaped booms or "sonic thumps" on communities. As an example, if the metrics follow a normal distribution, then knowledge of the distribution follows directly from knowledge of the first two statistical moments.

The purpose of this paper is to answer these questions by examining the statistical moments and distributions of sonic boom loudness metrics in a field of homogeneous isotropic turbulence. Data for the statistical moments will be obtained by simulating the propagation with a one-way equation. Two sonic boom waveforms are considered. The first is a typical sonic boom N-wave, and the second a shaped waveform. The distributions of the loudness metrics are examined and compared to the theoretical normal distribution to determine the normality of the loudness metrics. This is a difficult problem to address with flight tests and laboratory experiments because they are costly and significant data must be acquired to compute the distribution. However, numerical simulations are particularly suited to generate enough data to compute a probability distribution as well as converged statistical moments. Results indicate that the probability distributions of some of the loudness metrics are initially normally distributed, but become increasingly skewed to the right of a normal distribution as the propagation distance through turbulence increases. We also find that, for an appropriate scaling parameter, the statistics of the loudness metrics show similarity along

the propagation direction. In particular, the standard deviation of the Mark VII perceived level[13] collapses across all turbulence intensities considered.

The paper is organized as follows: Sec. II presents previous research on the propagation of sonic booms through turbulence and sonic boom loundess metrics. Section III presents the governing equation and computational method to propagate the sonic boom, as well as the method to synthesize the turbulent fields. In Sec. IV, the results of the simulations are presented. Section V provides a summary of the results presented and discusses future research.

## II. PREVIOUS WORK

### A. Metric Variability in Turbulence

Loubeau et al.[14] conducted a study of eleven different loudness metrics and their utility to accurately predict annoyance levels of shaped sonic boom signals. The study used data from seven different human response studies including five indoor studies and two outdoor studies. Results showed that five loudness metrics are highly correlated with human annoyance levels. These five metrics are the Mark VII perceived level (PL),[13] the B, D, and E weighted sound exposure levels, and the Indoor Sonic Boom Annoyance Predictor (ISBAP). In this paper, we focus on results for PL, ISBAP, BSEL, and ESEL. Bradley et al.[15] conducted a study of N-wave propagation through turbulence in the ABL using the Penn State KZKFourier code.[9] The study consisted of 96 different conditions that correspond to different levels of turbulence intensity, boundary layer height, propagation angle, and humidity. Simulation results showed that the standard deviations of PL and ISBAP increased with increasing turbulence intensity. However, the average values of both metrics were shown to decrease with increasing turbulence levels. Lipkens and Blackstock[11] showed experimentally that an N-wave in a turbulent field will have increased rise time with propagation distance, compared to a quiescent medium. Bradley et al.[15] suggested that this effect is the reason for the decrease in average PL and ISBAP with increasing turbulence intensity.

### B. Experimental Studies

Experiments have been performed in a laboratory setting to study the effects of turbulence on the distortion of "model" sonic boom waveforms generated by electric sparks. Davy and Blackstock[16] investigated the distortion caused by gas-filled soap bubbles on a model N-wave. The soap bubbles were separately filled with argon and helium gases to act as a converging lens and diverging lens, respectively. Davy and Blackstock[16] showed that the argon-filled bubble gave rise to N-wave peaking, while the helium-filled bubble led to N-wave rounding. At least qualitatively, the results indicated that peaking and rounding in an N-wave can occur when it passes through a medium with variable index of refraction, supporting Pierce's[17] explanation of the focusing and defocusing of the sonic boom waveform caused by turbulence.

The random focusing of an N-wave passing through a medium with variable index of refraction could explain the formation of caustics found in several laboratory experiments on propagation through turbulence.[12,18,19] An experiment by Ribner et al.,[18] published soon after the findings of Davy and Blackstock,[16] demonstrated the peaking and rounding effects on a model N-wave propagating through a turbulent jet. Their experiment indicates qualitatively the effect that turbulence can have on the N-wave amplitude. More recently, experiments by Ollivier and Blanc-Benon[19] and Averiyanov et al.[12] of model N-waves propagating through planar turbulent jets found the appearance of random caustics. This appearance of random caustics is explained as the random focusing effect of the turbulence on the N-wave, by Averiyanov et al.[12]

### C. Numerical Studies

Dagrau et al.[20] formulated a numerical approach for computing nonlinear acoustic propagation in a 2D heterogeneous medium. A one-way propagation method, called the HOWARD method, was validated with several acoustic benchmark problems. Their method has the advantage of accurately computing diffraction effects on the waveform compared to ray-based or parabolic methods. Yuldashev et al.[8] performed a 2D computational study of N-wave propagation in an isotropic turbulent field with a KZK-type equation.[21,22] Yuldashev et al.[8] found that the mean and standard deviation of maximum pressure follow a similar curve as a function of the normalized propagation distance, and that the standard deviation increases linearly for small propagation distance. The results further indicate the similarity of the problem with respect to the refraction length of a random phase screen and the rms index of refraction of the turbulent field. Luquet[10] later expanded the work of Dagrau et al.[20] to examine in 3D the effects of turbulence on sonic booms. More recent numerical studies by Leconte et al.[23–25] have shown that low-boom waveforms are less sensitive to atmospheric turbulence, and that 3D numerical simulations are slightly better at predicting the peak overpressure distribution compared to 2D simulations. Specifically, the 3D simulations are better at predicting occurrences of high amplification of the peak overpressure.

Stout[9] examined N-wave and shaped boom propagation through turbulence generated by a random Fourier modes approach developed by Blanc-Benon.[26] The turbulent fields that Stout[9] generates have an rms velocity that varies in the vertical direction to account for the inhomogeneity in the ABL. The PL and ISBAP distributions computed from the simulations agreed with measurements from the NASA Armstrong Flight Research Center (AFRC) sonic booms in atmospheric turbulence (SonicBAT) program.[15] The simulations performed by Stout[9] were used to develop a set of finite impulse response filters, using the approach of Locey and

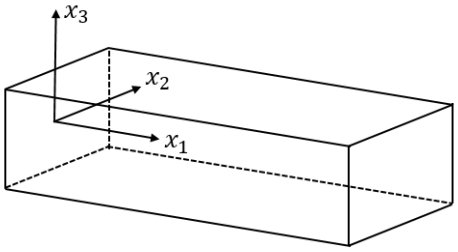


FIG. 1. Domain and coordinate system of the sonic boom simulations

Sparrow,[27] to artificially turbulize predicted waveforms that do not account for turbulence effects. Predictions of the mean and standard deviations of PL and ISBAP were then made for both N-waves and shaped booms using the filters.[9] Recently, Stout et al.[28] compared simulated PL distributions of N-wave propagation in the ABL to measurements taken at AFRC and NASA Kennedy Space Center (KSC). They found that a numerical approach with the KZK equation is able to predict most of the PL variances and only about half of the mean PL values of the measured waveforms. The simulated PL probability density distributions also compared favorably with the measured data, which shows that parabolic approaches for sonic boom are predictive near the ground.

In this investigation, we are motivated by recent numerical advancements for predicting sonic boom propagation in turbulence to conduct a parametric investigation of the effect of turbulence intensity on sonic boom loudness. We are interested in whether or not a scaling parameter exists for the propagation direction that incorporates the effect of turbulence on the waveform, such that the loudness metrics can be investigated as a function of this parameter. Previous investigations have examined sonic boom overpressure and rise time as a function of a scaled propagation distance (Yuldashev et al.[8]), but have not examined loudness metrics as a function of a scaled distance. Additionally, as will be shown in Sec. IV A, previous scaling parameters appearing in the literature are not suitable for small turbulence rms velocities or do not account for varying integral length scale. The length scale proposed in this investigation will attempt to remedy these previous shortcomings.

## III. COMPUTATIONAL APPROACH

Our computational approach assumes that the sonic boom is, locally, a superposition of plane waves as it approaches the top edge of the ABL. Each waveform is prescribed on the $x_1 = 0$ plane shown in Fig. 1, where $x_1$ is the propagation direction. The transverse directions are $x_2$ and $x_3$. The domain considered is a rectangular box of turbulence (Fig. 1).

### A. Governing Equation

A sonic boom waveform propagating through a turbulent flow is governed by the Navier-Stokes equations, along with the equations of energy and state. Coulouvrat[29] considered the propagation of an acoustic waveform in a medium with a low ambient Mach number and performed a decomposition of the governing equations. He was then able to derive a scalar governing equation for the acoustic pressure,

$$\frac{1}{\breve{c}^2}\frac{\breve{D}^2 p}{\breve{D}t^2} - \breve{\rho}\frac{\partial}{\partial x_i}\left(\frac{1}{\breve{\rho}}\frac{\partial p}{\partial x_i}\right) = -2\frac{\partial \breve{u}_j}{\partial x_i}\int_{-\infty}^{t}\frac{\partial^2 p}{\partial x_i \partial x_j}dt' + \frac{\delta}{\breve{c}^4}\frac{\breve{D}^3 p}{\breve{D}t^3} + \frac{\beta}{\breve{\rho}\breve{c}^4}\frac{\breve{D}^2 p^2}{\breve{D}t^2}, \quad (1)$$

that is accurate to second order in acoustic Mach number (or alternatively the Mach number of the mean flow), $\overline{c}^{-1}\partial_t \delta_p(x_i, t)$, where $\delta_p(x_i, t)$ is the particle displacement associated with an acoustic perturbation. The breve symbol $\breve{q}$ denotes a variable associated with the hydrodynamic component of the fluid. The flow variables can be further decomposed into mean variables $\overline{q}$ and turbulent fluctuations $q'$. Mean pressure, density, velocity, and the speed of sound are represented by $\overline{p}$, $\overline{\rho}$, $\overline{u}$, and $\overline{c}$, respectively. Turbulent velocity is indicated by $u_i'$. The acoustic pressure is denoted with $p$ and the time is represented by $t$. The coefficient of nonlinearity is $\beta$; for a gas, this is defined by $\beta = (\gamma + 1)/2$. The diffusivity of sound ($\delta$) is defined by Lighthill.[30] The material derivative operator in Eqn. 1 includes the turbulent velocity in the convective term,

$$\frac{\breve{D}}{\breve{D}t} = \frac{\partial}{\partial t} + \breve{u}_i\frac{\partial}{\partial x_i}. \quad (2)$$

Of interest in this paper is to capture the effects of the velocity fluctuations on the sonic boom waveform. Therefore, the terms with mean flow, density fluctuations, and fluctuations of the speed of sound are eliminated from Eqn. 1. Thermoviscous absorption and molecular relaxation of the medium is not considered, to isolate the attenuation effect due to turbulence. Additionally, the medium of propagation is not stratified so the mean density and speed of sound are constant in the domain. The integral length scales ($L_f$, see Batchelor[31] for definition) of the turbulent field considered here vary from 80 to 200 m. For these scales, the spatial derivatives of the turbulent velocity scale as $u'/L_f$ and are generally an order of magnitude less than $u'$. This was verified numerically when we calculated the spatial derivatives of the velocity fluctuations. Therefore, we neglect the spatial derivatives of the velocity fluctuations. Applying these assumptions, Eqn. 1 can be rewritten as,

$$\frac{\partial^2 p}{\partial t^2} - \overline{c}^2\frac{\partial^2 p}{\partial x_i \partial x_i} = -2u_i'\frac{\partial^2 p}{\partial x_i \partial t} + \frac{\beta}{\overline{\rho}\overline{c}^2}\frac{\partial^2 p^2}{\partial t^2}, \quad (3)$$

which is a wave equation with perturbation terms on the right-hand side. In order to compute the forward solution, Eqn. 3 must be written in terms of the delayed time

$\tau = t - \overline{c}^{-1} x_1,$

$$\frac{\partial^2 p}{\partial x_1 \partial \tau} = \frac{\overline{c}}{2}\frac{\partial^2 p}{\partial x_i \partial x_i} + \frac{u_1'}{\overline{c}^2}\frac{\partial^2 p}{\partial \tau^2} - \frac{u_i'}{\overline{c}}\frac{\partial^2 p}{\partial x_i \partial \tau} + \frac{\beta}{2\overline{\rho c}^3}\frac{\partial^2 p^2}{\partial \tau^2}. \quad (4)$$

Equation 4 is a partially one-way equation, and the forward solution is computed numerically in our simulations. Each physical effect is solved independently and the solution is composed with a Strang[32] split-step method. The terms in Eqn. 4 are split into several groups representing different physical effects. This is the approach that Luquet[10] adapted to solve Eqn. 4, where the composed solution for the acoustic pressure is

$$p\left(x_1 + \Delta x_1\right) = p^N_{\frac{\Delta x_1}{2}} \circ p^H_{\frac{\Delta x_1}{2}} \circ p^D_{\Delta x_1} \circ p^H_{\frac{\Delta x_1}{2}} \circ p^N_{\frac{\Delta x_1}{2}}, \quad (5)$$

and $\circ$ is the composition operator. The superscripts $N, D$, and $H$ indicate terms representing the solution involving nonlinear, diffraction, and heterogeneous effects. The first term on the right-hand side of Eqn. 4 contains the diffraction effects. The next two terms are heterogeneous terms that account for the effects of turbulent velocity fluctuations on the waveform. The last term in Eqn. 4 represents nonlinear distortion.

The methods used to independently compute the diffraction, heterogeneous effects, and nonlinear effects are adapted from previous numerical approaches by Luquet[10] and Stout.[9] The diffraction effects are computed exactly in the forward direction using the angular spectrum method.[10,33] The heterogeneous terms are split into two groups. The first group involves only terms with derivatives of the acoustic pressure in $\tau$ or $x_1$. The governing equation for this first group can be solved exactly for the forward propagating step, and the solution is incorporated into the nonlinear computation following the procedure of Stout.[9] The second group contains heterogeneous terms with derivatives of the pressure in the transverse directions. Variability of the turbulent field and subsequently the waveform in the transverse directions lead to wavefront folding.[3,34] Stout[9] integrates these terms with an implicit backward finite difference method. In this work, we adopt the same approach but integrate these terms with the Crank-Nicolson[35] scheme because of the unconditional stability of the method. The nonlinear effects are governed by the inviscid Burgers' equation. The algorithm implemented to solve the inviscid Burgers' equation is outlined by Hayes[36] and generalized to nonquadratic nonlinearities by Coulouvrat.[37]

### B. Simulation Parameters and Velocity Fields

We consider the propagation of two waveforms, a simulated shaped low-boom waveform from the NASA X-59 C609 aircraft and an N-wave of similar amplitude. The NASA low-boom waveform is computed from a design iteration of NASA's X-59 QueSST aircraft at a free-stream Mach number of 1.40 at an altitude of 54,000 ft.[38]

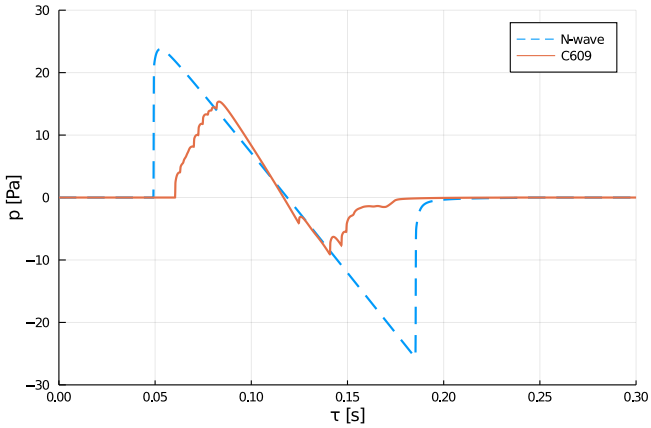


FIG. 2. The two initial waveforms considered, prescribed at the $x_1 = 0$ plane. The N-wave (dashed line), and the simulated low-boom waveform from the NASA X-59 C609 aircraft (solid line). Both waveforms shown in the figure have been propagated by PCBoom[40] to just above the atmospheric boundary layer region.

The N-wave was computed by PCBoom for a cruising altitude of 54,000 ft, to match the low-boom on-design cruising altitude, and no ground reflection factor was applied which led to an amplitude similar to that of the low-boom waveform. For the simulations considered here, the waveforms are initially propagated to the top of the ABL by PCBoom.[7,39,40] Then, the PCBoom output waveforms are resampled with Lanczos resampling to prevent Gibb's phenomenon at the shocks and prescribed as inputs to the simulations performed here. Figure 2 shows the output waveforms from PCBoom, which are then resampled and prescribed at $x_1 = 0$ m. Both waveforms are sampled at 12 kHz.

The computational domain is discretized by a uniform grid. The spatial step size in the $x_1$ direction is 2 m. The transverse directions are 1022 m in length, and the distance between grid points is 2 m. A study was conducted to ensure that the results converge when the grid is refined from 8 m spacing to 4 m and then to 2 m. The Taylor microscale of the generated fields is approximately $\lambda_t = 5$ m for all simulations. Therefore, with the chosen grid size, the turbulent field is sampled at approximately $(2/5)\lambda_t$. Periodic boundary conditions are implemented at the transverse boundaries.

The parameter space of the simulations is meant to mimic the turbulence fluctuation intensities and length scales found in the ABL. Klipp[41] shows that integral scales over flat-terrain can vary between 80 to 250 m at approximately 50 m above ground during the daytime, and 15 to 60 m during a near-neutral night. For the current study, the longitudinal integral scale ($L_f$) was prescribed to be 100 m, which mimics a daytime condition. Turbulence measurements taken at AFRC during the SonicBAT flight test indicate that the turbulence rms velocity ranged from 0.35 m/s $< u_{\text{rms}} <$ 2.45 m/s. Based

on the range of rms velocities in SonicBAT, the rms velocity was varied in our simulations between 0.20 m/s and 3.0 m/s in an increment of 0.40 m/s.

The method of Frehlich[42] is used to generate the turbulent velocity fields. This method simulates all three velocity components of the field and accounts for the cross-spectral densities between each component. The three dimensional velocity field, according to Monin and Yaglom,[43] can be represented by the Fourier-Stieltjes integral

$$u_i'(\mathbf{x}) = \int_{-\infty}^{\infty} \exp(-i\mathbf{k}\cdot\mathbf{x})\, dZ_i(\mathbf{k}), \tag{6}$$

where $Z_i$ is the spectral contribution of component $i$. The functions $Z_i$ are the Fourier modes of each velocity component. By making use of the relation,

$$\overline{dZ_i(\mathbf{k})\, dZ_j^*(\mathbf{k}')} = \delta(\mathbf{k}-\mathbf{k}')\,\Phi_{ij}(\mathbf{k})\, d\mathbf{k}d\mathbf{k}', \tag{7}$$

where $\delta$ is the Dirac delta function, we are able to model the Fourier modes. Equation 7 shows that the Fourier modes are directly related to the velocity spectrum $\Phi_{ij}$. The relation between the energy spectrum $E$ and the velocity spectrum $\Phi_{ij}$ for an incompressible flow is,

$$\Phi_{ij}(\mathbf{k}) = \frac{E(k)}{4\pi^2 k^4}\left(k^2\delta_{ij} - k_i k_j\right). \tag{8}$$

We chose to model $\Phi_{ij}$ with the von Kármán composite spectrum,[44,45]

$$E^{vK}(k) = \frac{4\Gamma(17/6)}{\sqrt{\pi}\Gamma(1/3)}\frac{u_{\text{rms}}^2 k^4 L_0^5}{(1+k^2L_0^2)^{17/6}}. \tag{9}$$

Here, $\Gamma$ is the gamma function, and $u_{\text{rms}}$ is the rms velocity of the turbulence. The outer scale $L_0$ is related to the integral length scale by the expression,

$$L_0 = \frac{\Gamma(1/3)}{\sqrt{\pi}\Gamma(5/6)} L_f. \tag{10}$$

The expression to model the Fourier modes of the longitudinal velocity component is the square root of the velocity spectrum multiplied by a set of uncorrelated complex random numbers ($N_1$) drawn from a uniform distribution with zero mean and variance equal to 1,

$$dZ_1(\mathbf{k}) = N_1(\mathbf{k})\sqrt{\Phi_{11}^{vK}(\mathbf{k})}dk_1dk_2dk_3. \tag{11}$$

This ensures that the average of the Fourier modes multiplied by their complex conjugate is equal to $\Phi_{11}^{vK}(\mathbf{k})\, dk_1dk_2dk_3$ only when $\mathbf{k}=\mathbf{k}'$.

The $u_1$ velocity component is generated by taking the inverse Fourier transform of $N_1(\Phi_{11}^{vK}(\mathbf{k}))^{1/2}$. However, to generate all three velocity components, we must account for the cross-spectral density. This can be achieved by modeling the Fourier modes by,

$$\begin{bmatrix} dZ_1 \\ dZ_2 \\ dZ_3 \end{bmatrix} = \begin{bmatrix} H_{11} & 0 & 0 \\ H_{12} & H_{22} & 0 \\ H_{13} & H_{23} & H_{33} \end{bmatrix} \begin{bmatrix} N_1 \\ N_2 \\ N_3 \end{bmatrix}, \tag{12}$$

where the $H$ matrix is given by Shinozuka[46] as a function of the model velocity spectrum $\Phi_{ij}^{vK}$. The velocity field is generated by computing the inverse Fourier transform of each Fourier mode.

Each velocity field is categorized by a longitudinal integral scale and rms velocity. The longitudinal integral scale is the integral of the longitudinal correlation function,

$$L_f = \int_0^{\infty} f(r)dr, \tag{13}$$

and the lateral integral scale ($L_g$) is the integral over the lateral correlation function. This is related to $L_f$ by the expression of $g$ given by Batchelor,[31]

$$L_g = \int_0^{\infty} g(r)dr = \frac{1}{2}L_f. \tag{14}$$

Wilson[47] gives expressions for the longitudinal and lateral correlations ($f^{vK}$ and $g^{vK}$) based on the von Kármán model (Eqn. 9). For validation purposes, the computed correlations of the generated fields were compared to the expressions of $f^{vK}$ and $g^{vK}$. For each specific $u_{\text{rms}}$ and $L_f$ value, we generate 25 random realizations of the three-dimensional velocity field. Figure 3 displays the average computed correlations for $u_{\text{rms}} = 1.03$ m/s and $L_f = 106.2$ m of the N-wave simulations alongside $f^{vK}$ and $g^{vK}$. The relative error of $f$, defined as the L2 norm of the error normalized by the L2 norm of $f^{vK}$, is 0.09, which indicates good agreement. The relative error of $g$ is 0.08, which is consistent with the error for the longitudinal correlation.

In Table I, the longitudinal and lateral length scales are shown along with the variance of each velocity component for the N-wave simulations. Each case corresponds to a rms velocity setpoint (e.g., for case 2, $u_{\text{rms}} = 0.2$ m/s) and 25 different realizations of the velocity field are generated for each setpoint. Then, once the fields have been generated, the length scales and rms velocity are computed and averaged across each realization to find the true setpoint values. These values provide a quantitative measure of the isotropy of the generated fields. For isotropic turbulence, $L_g = 0.5L_f$. The ratio $L_f/L_g$ for each case is within a range of $2.00 \pm 0.26$, except for case 8 where $L_f/L_g = 1.33$. The length scales and $u_{\text{rms}}$ of the turbulent fields generated for the low-boom propagation cases are given in Table II. The most significant deviation in the ratio $L_f/L_g$ from a value of 2 is $L_f/L_g = 2.49$ for case 5.

By generating the turbulence with a von Kármán energy spectrum, we make an assumption of homogeneity and isotropy. In general, ABL turbulence near the ground is inhomogeneous, especially in windy conditions.[48] However, in calm sunny day conditions, homogeneous turbulence is a suitable approximation of bouyancy driven turbulence in the ABL, for the purposes of sonic boom propagation studies. In practice, the results we obtain are limited to calm sunny day conditions due to these underlying assumptions of the turbulent fields that are generated. The purpose of making these

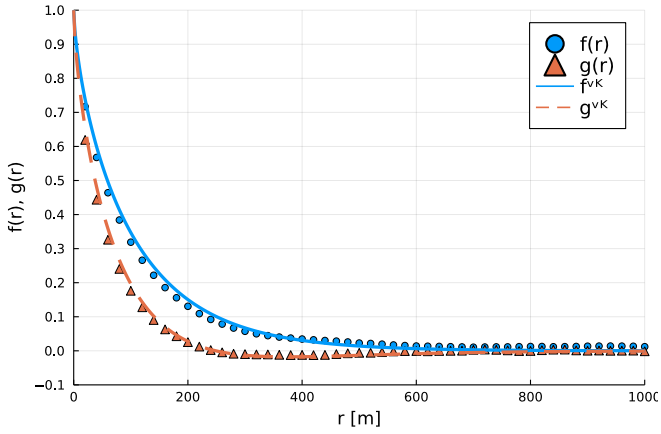


FIG. 3. Comparison of the average computed longitudinal (circles) and lateral (triangles) correlations for all 25 fields with $u_{\text{rms}} = 1.04$ m/s and $L_f = 106.2$ m compared to the correlation functions of the von Kármán model (solid and dashed lines).

TABLE I. Computed integral scales and rms velocity of the turbulent fields generated for the N-wave simulations.

| Case | $L_f$ (m) | $L_g$ (m) | $L_f/L_g$ | $u_{\text{rms}}$ (m/s) |
|---|---|---|---|---|
| 1 | 0.0 | 0.0 | NA | 0.0 |
| 2 | 88.9 | 43.9 | 2.03 | 0.22 |
| 3 | 91.8 | 41.5 | 2.21 | 0.62 |
| 4 | 106.2 | 50.1 | 2.12 | 1.03 |
| 5 | 86.7 | 48.0 | 1.81 | 1.44 |
| 6 | 108.2 | 52.1 | 2.08 | 1.90 |
| 7 | 89.7 | 51.5 | 1.74 | 2.29 |
| 8 | 81.8 | 61.5 | 1.33 | 2.72 |
| 9 | 88.2 | 44.2 | 1.99 | 3.05 |

TABLE II. Computed integral scales and rms velocity of the turbulent fields generated for the low-boom simulations.

| Case | $L_f$ (m) | $L_g$ (m) | $L_f/L_g$ | $u_{\text{rms}}$ (m/s) |
|---|---|---|---|---|
| 1 | 0.0 | 0.0 | NA | 0.0 |
| 2 | 79.8 | 49.0 | 1.63 | 0.21 |
| 3 | 89.4 | 42.8 | 2.08 | 0.61 |
| 4 | 78.6 | 32.0 | 2.45 | 1.04 |
| 5 | 94.6 | 38.0 | 2.49 | 1.47 |
| 6 | 93.4 | 45.2 | 2.07 | 1.86 |
| 7 | 80.8 | 42.2 | 1.91 | 2.39 |
| 8 | 96.6 | 56.3 | 1.72 | 2.62 |
| 9 | 77.8 | 43.5 | 1.78 | 3.15 |

assumptions is the ability to formulate a length scale to examine the problem on a non-dimensional basis, which is discussed further in Sec. IV.

## IV. RESULTS AND DISCUSSION

The results for cases 2 through 9 are presented below. In Sec. III B, it was mentioned that the nominal waveforms were resampled with Lanczos resampling before being used as input to the simulations, in order to avoid Gibb's oscillations in the computations. The nominal condition refers to the initial N-wave or low-boom waveform and is denoted with a subscript nom. The process of resampling the nominal waveform introduces a small amount of numerical dissipation to the waveforms before conducting the simulations. This dissipation was recognized as a complicating factor in estimating the nominal waveform. To address this, we do not consider the average noise metric values in section IV E but rather the average decrease in the noise metrics from the nominal condition. Thus, the results hold whether the nominal metric values are computed directly from the PCBoom output or the resampled waveforms. Simulations were also performed without turbulence to verify that the effect of nonlinear distortion of the waveforms on the noise metrics are relatively small. It was found that, for both waveforms, the PL metric value changes by no more than 2% of its initial value due to nonlinear distortion. Since atmospheric absorption is not considered and the nonlinear distortion that each waveform in Fig. 2 experiences is small, we assume that the overpressure and metric values are equal to the nominal condition at every location in the domain in the case of no turbulence.

### A. Length Scale

We examine predictions on a nondimensional basis. Appropriate nondimensional parameters for the problem should include the effects of the fluctuation intensity and turbulent length scales, and collapse the predictions appropriately. In order to determine the appropriate length scale to nondimensionalize the results by, we consider three different length scales, two of which have appeared previously in the literature for wave propagation through turbulence. The caustic distance scale $2\sqrt{\pi}^{-1} L_f \sigma_{KW}^{-2/3}$ of Kulkarny and White[49] is the first length scale considered. Kulkarny and White[49] determined through the use of geometrical acoustics that caustics occur on a distance scale of $2\sqrt{\pi}^{-1} L_f \sigma_{KW}^{-2/3}$, where

$$\sigma_{KW}^2 = \int_{-\infty}^{\infty} \frac{\partial^4}{\partial r_2^4} R_{11}(r_1, 0)\, dr_1, \tag{15}$$

is the scaling factor suggested by Kulkarny and White, $r_1$ is the longitudinal separation distance, $r_2$ is the lateral separation distance, and $R_{11}$ is the longitudinal correlation. The standard deviation of the ray directions is $\sigma_{KW}^{2/3}$.

Blanc-Benon et al.[50] consider the case of a Gaussian correlation of the turbulent velocities. After integration with the Gaussian correlation, the expression for $\sigma_{KW}^{2/3}$ becomes

$$\sigma_{KW}^{2/3} = \frac{60^{1/3} u_{\text{rms}}^{2/3} \pi^{1/6}}{L}, \tag{16}$$

where $L = 2\sqrt{\pi}^{-1} L_f$.

The distance scale $2\sqrt{\pi}^{-1} L_f \sigma_{KW}^{-2/3}$ is limited to waves with a wavelength less than a typical length scale of the turbulence. The wavelength for the N-wave in our simulations is approximately $\lambda = 51$ m, with $\bar{c} = 343$ m/s. The assumption of Kulkarny and White[49] that $\lambda << L_f$ is not satisfied for the simulations considered here, where $L_f$ varies between 77.8 and 108.2 m. In Fig. 4, the probability density functions of the location of the first caustic along the propagation direction are plotted for cases 3-9 of the N-wave simulations. The location of the first caustic in our simulations was determined to be the first location along the propagation axis at each transverse location where $\Delta p > 1.5\Delta p_{\text{nom}}$, and $\Delta p$ is the maximum overpressure.

Although the small wavelength assumption of Kulkarny and White is not satisfied for our simulations, we see in Fig. 4 that for $u_{\text{rms}} \geq 1.8$ m/s (cases 6-9) the distance to the first caustic ($x_{\text{caust}}$) in our simulations agreed with the results of Kulkarny and White.[49] The maximum of the PDF for cases 6 through 9 occur near the same location of the maximum of the Kulkarny and White result, $x_1 \sigma_{KW}^{2/3} L^{-1} = 1.3$. However, for cases 3 and 4, the computed PDFs do not agree with the Kulkarny-White prediction, and thus motivated the search for a different scaling distance. For case 3, the computed PDF has a peak at $x_1 \sigma_{KW}^{2/3} L^{-1} = 3.75$, and for both cases 3 and 4, the probability of a caustic occurring beyond $x_1 \sigma_{KW}^{2/3} L^{-1} = 5$ is larger than the Kulkarny-White prediction. This disagreement between the computed PDFs and the Kulkarny and White[49] prediction at lower $u_{\text{rms}}$ values cause the scalar statistics of the loudness metrics for these cases to have significant disagreement with cases 6 through 9 along $x_1 \sigma_{KW}^{2/3} L^{-1}$.

Yuldashev[8] considers the refraction length $x_r$ behind a random phase screen with Gaussian correlation length, which is inversely proportional to the standard deviation of the ray directions. Using a one-dimensional random phase screen to represent the turbulence, Rudenko and Enflo[51] determined that the standard deviation of the overpressure $\sigma_{\Delta p}$ increases linearly according to $\sigma_{\Delta p} = 0.5 x_1 x_r^{-1}$ before reaching a maximum value. Yuldashev[8] assumes this relationship to be true for each turbulent condition to find the dependence of $x_r$ on the rms velocity $u_{\text{rms}}$. Yuldashev[8] determined from linear regression of each simulation to satisfy $\sigma_{\Delta p} = 0.5 x_1 x_r^{-1}$ that $x_r$ has the following dependence on the rms velocity,

$$x_r = 0.8 \left( \frac{0.01 \bar{c}}{u_{\text{rms}}} \right)^{0.9}. \tag{17}$$

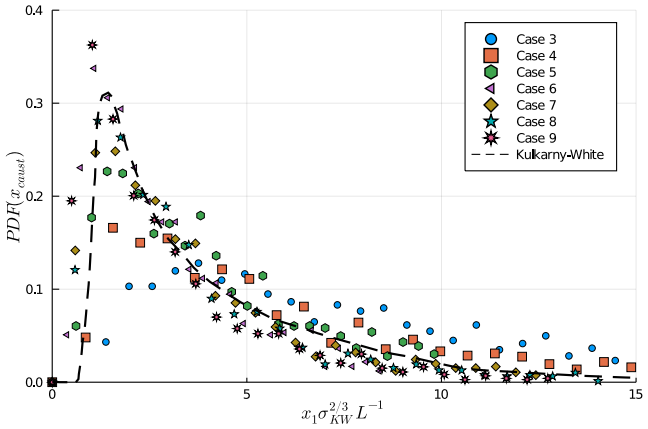


FIG. 4. Probability density functions of the first occurrence of a caustic $P(\Delta p > 1.5\Delta p_{\text{nom}})$, computed from simulations, compared to the results of Kulkarny and White[49] (dashed line).

Equation 17 assumes $\sigma_{\Delta p} = 0.5 x_1 x_r^{-1}$ is true for all simulations, however, the expression was determined with geometrical acoustics for a one-dimensional random phase screen with a Gaussian correlation. Turbulence is three-dimensional in nature, is not a Gaussian process, and the geometrical acoustics assumption is not applicable for our simulations where the wavelength is close to the integral scale of the turbulence. For this reason, we do not use $x_r$ to nondimensionalize our results.

Pierce[17] suggests that rippling in the wavefront, caused by inhomogeneities in the medium, leads to random focusing and defocusing. We propose a new length scale to account for the average effect of the turbulent field on the random focusing of the sonic boom. Davy and Blackstock[16] demonstrated qualitatively the focusing and defocusing effect on an N-wave by a spherical inhomogeneity. In the turbulent field, there will be velocity perturbations that focus the wave and some that defocus the wave. In previous research,[8,50] the rms refraction index $u_{rms} \bar{c}^{-1}$ appears in the expressions of length scales used to nondimensionalize simulation results. In the length scale proposed here, the rms refraction index of the velocity fluctuations will be the parameter used to quantify the impact of turbulence intensity on the random focusing of the wave.

We consider a spherical lens, where the index of refraction is

$$n = 1 + \frac{u_{\text{rms}}}{\bar{c}}. \tag{18}$$

The location of the focus is

$$\ell_f = \frac{1}{2} \frac{na}{n-1}, \tag{19}$$

where $a$ is the radius of the lens. For a turbulent medium, we assume that the radius of the lens would be a function of some length scale $L_c$ of the turbulent flow, $a = F(L_c)$. It is not clear what the length scale of the flow should be, or what the form of $F$ should look like. We propose

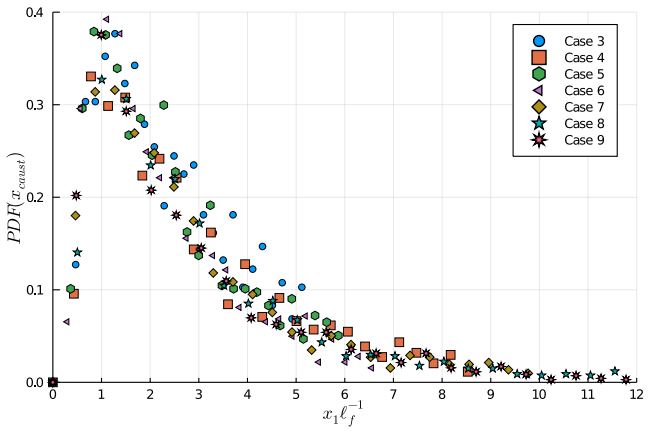


FIG. 5. Probability density functions of the first occurrence of a caustic $P(\Delta p > 1.5\Delta p_{\text{nom}})$, computed from simulations, along the scaled propagation distance $x_1\ell_f^{-1}$.

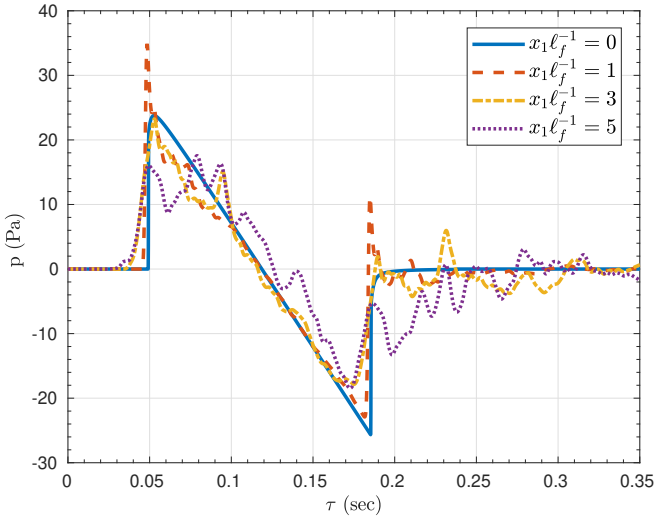


FIG. 6. Sample waveforms at different $x_1\ell_f^{-1}$ locations for case 6 of the N-wave simulations.

to approximate the relationship between the length scale and the radius a as linear and set $L_c = L_f$. By doing so, we assume that the focusing distance and integral length scale are directly proportional when the rms velocity and sound speed are held fixed. The radius $a$ is thus expressed as,

$$a = C_1 L_f. \tag{20}$$

The resulting form of $\ell_f$ is then

$$\ell_f = \frac{C_1 L_f}{2} \frac{\overline{c} + u_{\text{rms}}}{u_{\text{rms}}}, \tag{21}$$

where $C_1$ is the constant of proportionality. This constant was chosen to be 0.065 so that the most probable location of the first caustic will occur at $x_1/\ell_f = 1$.

When the integral scale is held constant, $\ell_f$ changes only when $\overline{c}/u_{\text{rms}}$ varies. The proportionality of $\ell_f$ to $\overline{c}/u_{\text{rms}}$ is actually quite close to the expression of the refraction length (Eqn. 17), which is proportional to the same quantity raised to 0.9. Additionally, it should be noted that Pierce and Maglieri[3] suggest the radius of curvature of a ripple in the wavefront caused by a velocity perturbation $u'$ is proportional to $\overline{c}/u'$ when the length scale is held constant.

The PDF of the location of the first caustic for each simulation was computed for the scaled propagation distance $x_1\ell_f^{-1}$ and plotted in Fig. 5. The computed PDF of each case has a maximum in the range $0.83 \leq x_1\ell_f^{-1} \leq 1.27$. Previously, the maximum PDF location for the results scaled by the Kulkarny-White scale were in a range from $1.0 \leq x_1\sigma_{KW}^{2/3}L^{-1} \leq 3.75$. Thus, the collapse of the PDFs with respect to $x_1\ell_f^{-1}$ shows improvement over the Kulkarny-White scaling (Fig. 4).

The benefit of the new parameter $\ell_f$ is its ability to consistently predict the maximum probable location of the first caustic across the entire range of rms velocities considered. The PDF of $x_{\text{caust}}$ was computed only for the N-wave simulations. This is because, for the low-boom waveform, the rise time is initially much longer and overpressure values that are 50% greater than the initial overpressure rarely occur. Although the PDF was not computed for the low-boom simulations, the parameter $\ell_f$ is used to scale the results of both waveforms. The collapse of the loudness metric data for both waveforms will be investigated further in Sec. IV E.

### B. Loudness

In the remainder of Sec. IV, the loudness levels and metric values are reported. These quantities are computed from waveforms extracted at 342 different $x_1$ locations for each simulation performed. At each $x_1$ location, 100 waveforms are extracted in the x2 and x3 directions, with each location separated from another by at least 100m. For each turbulence case, 25 simulations are performed. The averages of the loudness metrics computed along the propagation direction are thus determined from a set of 2500 different waveforms. Some sample waveforms extracted at different $x_1\ell_f^{-1}$ locations for the N-wave and low-boom waveform are shown in Figs. 6 and 7, respectively. These waveforms are extracted from the same transverse locations ($x_2$ and $x_3$). The N-waves in Fig. 6 illustrate the peaking and rounding effects.

The loudness for frequencies of 6.3 Hz to 5 kHz is computed at each $x_1\ell_f^{-1}$ location. The loudness for higher bands is not computed because these bands are above the Nyquist frequency. The sampling frequency of 12 kHz was determined based upon computational resources and comparisons to the loudness metrics computed with a sampling frequency of 34 kHz. The loudness metrics computed with a 12 kHz sampling frequency were found to be within ±0.2 dB of the metrics computed at higher sampling frequencies. The PL was computed following the procedure of Jackson and Leventhall.[52]

Figure 8 displays the average loudness in sones for each one-third octave band considered at different $x_1\ell_f^{-1}$

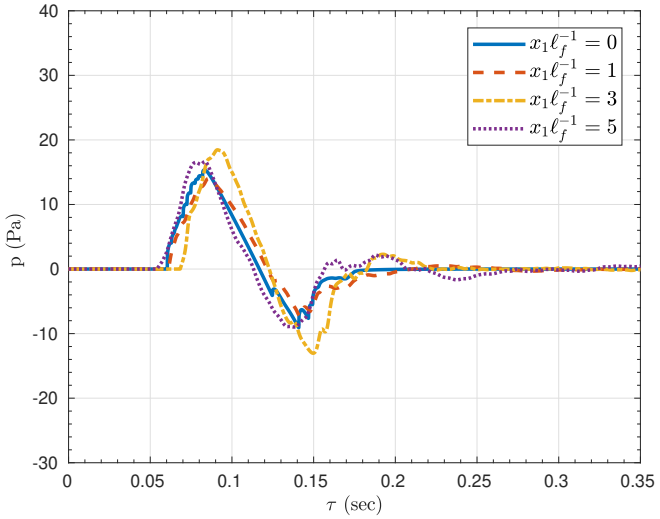


FIG. 7. Sample waveforms at different $x_1\ell_f^{-1}$ locations for case 6 of the low-boom simulations.

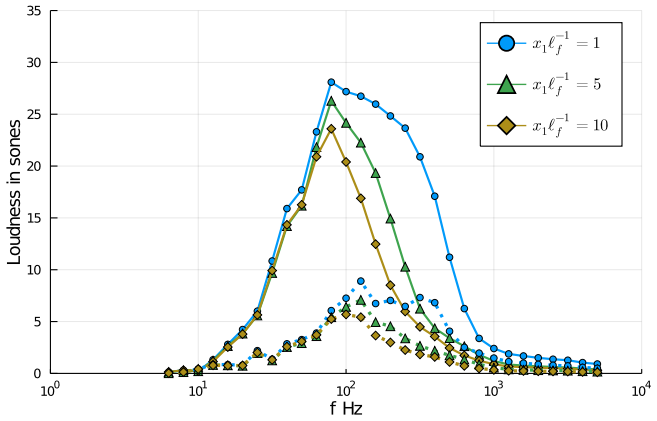


FIG. 8. Average loudness levels for the one-third octave bands in sones at case 9 for the N-wave (solid lines) and low-boom waveform (dotted lines).

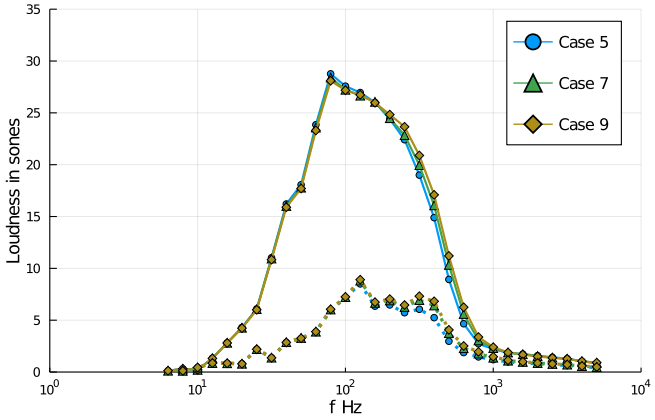


FIG. 9. Average loudness levels in sones at $x_1\ell_f^{-1} = 1$ for the N-wave (solid lines) and low-boom waveform (dotted lines).

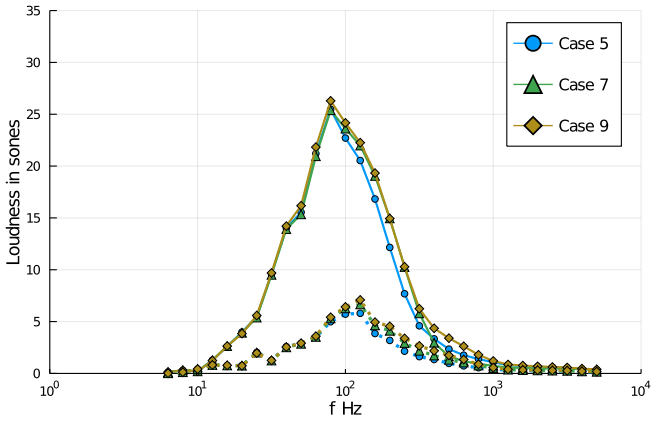


FIG. 10. Average loudness levels in sones at $x_1\ell_f^{-1} = 5$ for the N-wave (solid lines) and low-boom waveform (dotted lines).

locations. For both waveforms, the loudness for frequencies between 100 and 1000 Hz decreases significantly along $x_1\ell_f^{-1}$. Since $x_1\ell_f^{-1}$ represents the effective propagation distance through turbulence, the results indicate that turbulence reduces the loudness in the range of 100 to 1000 Hz, but has little effect on the loudness from 10 to 100 Hz. Physically, this is an indication that the turbulence more effectively reduces loudness in the 100 to 1000 Hz frequency range.

In Figs. 9 and 10, the one-third octave band loudness levels in sones are plotted for three different $u_{\text{rms}}$ levels with $x_1\ell_f^{-1}$ fixed at 1 and 5, respectively. When $x_1\ell_f^{-1}$ is held fixed and $u_{\text{rms}}$ is increased, there is a slight variation among the different loudness spectra, specifically between 100 and 1000 Hz. The spectra for both waveforms appear to show a better collapse with respect to the scaling distance $\ell_f$ for $x_1\ell_f^{-1} = 1$ rather than $x_1\ell_f^{-1} = 5$. This indicates that the loudness metrics may show a better collapse for small $x_1\ell_f^{-1}$ values.

### C. Probability Distributions of Loudness Metrics for the N-wave

Results from Stout[9] and Bradley et al.[15] indicate that the ΔPL is well approximated by a normal distribution after propagation through turbulence for the majority of probabilities. In this section, our results indicate that ΔPL is well approximated by a normal distribution for all probabilities up to a certain propagation distance that depends on the turbulence level. Here, ΔPL is the difference between the PL obtained from our simulations and the nominal, PL - $\text{PL}_{\text{nom}}$. The nominal PL is the PL at $x_1\ell_f^{-1} = 0$. Since we consider an ensemble of isotropic turbulent fields, ΔPL is a random variable and its average $\overline{\Delta\text{PL}}$ is a function of the propagation distance. It should be noted that the shape of the dis-

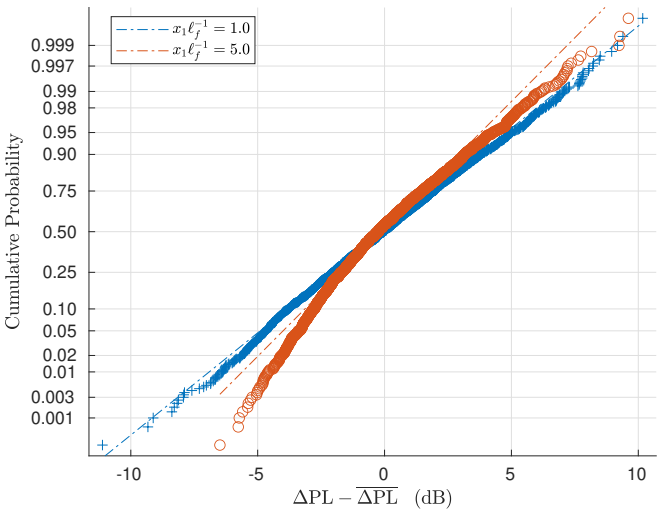


FIG. 11. Probability plots of ΔPL with respect to the average for case 9 of the N-wave simulations.

tribution computed for the delta values of each metric will be the same as the shape of the distribution of the metrics themselves, since we are simply normalizing by the nominal value. Thus, we can draw conclusions about the PL distribution by examining the ΔPL distribution, and so on for the other metrics considered. For a visual representation of the ΔPL distribution, the cumulative probability of $\Delta PL - \overline{\Delta PL}$ is shown in Fig. 11 at two $x_1\ell_f^{-1}$ locations. The dashed lines in Fig. 11 represent theoretical normal distributions, and the symbols represent the computed cumulative probabilities of the data. Figure 11 shows that as the value of $x_1\ell_f^{-1}$ increases, the distributions deviate more significantly from the normal distribution. Specifically, the probability of ΔPL being 3 to 8 dB lower than the average is lower than what is predicted for a normal distribution.

The deviation of the distribution from the theoretical normal distribution as $x_1\ell_f^{-1}$ increased was observed consistently across all rms velocities and loudness metrics considered (PL, ISBAP, BSEL, DSEL, and ESEL). Each metric has a tendency to skew to the right of a normal distribution as $x_1\ell_f^{-1}$ increases. It should be noted that ΔDSEL is skewed to the right of a normal distribution for $x_1\ell_f^{-1} > 0.5$, so it can only be approximated by a normal distribution only for very small $x_1\ell_f^{-1}$ values.

We examined the normality quantitatively by conducting hypothesis tests on the distributions of each metric along the propagation direction. The two tests considered to examine the normality of the distributions are the Anderson-Darling (AD)[53] and the Kolmogorov-Smirnov (KS)[54] tests. The p-value of each test was computed, and if the p-value was greater than the significance level (set to 0.05) then the distribution is considered to be normal. A significance level of 0.05 is commonly used in statistical studies.[55] It should be noted that the American Statistical Association has stated that, "Scientific conclusions and business or policy decisions should not be based only on whether a p-value passes a specific threshold."[55] For this reason, probability plots are provided as supplemental evidence to be used in conjunction with the hypothesis tests.

For each metric, except ΔDSEL, the hypothesis tests indicated that there was a value of $x_1\ell_f^{-1}$ for each case where the p-values past these locations are always below the significance level. We denote this location as the transition location $x_t$, where hypothesis tests indicate that for $x < x_t$ the metric can be considered normal and for $x > x_t$ we cannot draw the conclusion of normality. The p-values for ΔDSEL were below the significance level for $x_1\ell_f^{-1} > 0.5$ at all turbulence levels. The values of $x_t$ for ΔBSEL, ΔESEL, ΔISBAP, and ΔPL are presented in Tables III and IV. Each hypothesis test was conducted at an interval of $\Delta x_1\ell_f^{-1} = 0.1$, and the $x_t$ was determined to be the location where both hypothesis tests return p-values less than the significance level for $x_1 \geq x_t$. Tables III and IV show that the value of $x_t$ is fairly consistent across all metrics for each case. Since each test was conducted at an interval $\Delta x_1\ell_f^{-1} = 0.1$, each value of $x_t$ has the associated uncertainty of $\pm 0.1\ell_f$. The results indicate that to a good approximation, the loudness metrics are no longer normally distributed for $x_1\ell_f^{-1} > 2.5$. In terms of the physical distance $x_1$, the transition locations decrease as the rms velocity increases. At the same dimensional propagation distance, $x_1$, the distributions of the loudness metrics will become increasingly skewed from a normal distribution as the turbulence intensity increases.

It should be noted that the hypothesis tests conducted here examine the normality of the distribution for all cumulative probabilities, and that our results are in agreement with that of Stout.[9] Qualitative examination of the probability distributions of PL and ISBAP obtained by Stout[9] for low, medium and high intensity turbulence shows that as the turbulence intensity increases (i.e., increasing $u_{\text{rms}}$) the distributions skew increasingly further to the right of a normal distribution. In fact, for the vast majority of the N-wave data, Stout[9] states that the normal distribution closely approximates the simulation data from 5-10% cumulative probability up to 90-95% cumulative probability. Even for the highest $u_{\text{rms}}$ case considered (case 9) in our simulations, Fig. 11 shows that at $x_1\ell_f^{-1} = 5$, the distribution follows a normal distribution between 10% and 95% cumulative probability. Thus, the results presented here appear to be consistent with previous results from numerical simulations.

### D. Probability Distributions of Loudness Metrics for the Shaped Waveform

Distributions of the ΔPL and ΔISBAP for the low-boom waveform are similar to those computed for the N-wave. In Fig. 12, the ΔPL probability distribution closely follows a normal distribution for $x_1\ell_f^{-1} = 1$. At $x_1\ell_f^{-1} = 5$, the distribution is skewed to the right of a normal distribution, which is consistent with the N-wave results.

TABLE III. Values of the transition location ($x_t$) for PL and ISBAP for cases 3, 5, 7, and 9.

| Case | ΔPL | ΔISBAP |
|---|---|---|
| 3 | $2.3\ell_f$ (3803.1 m) | $2.4\ell_f$ (3968.5 m) |
| 5 | $2.1\ell_f$ (1415.4 m) | $2.4\ell_f$ (1617.6 m) |
| 7 | $2.4\ell_f$ (1054.9 m) | $2.4\ell_f$ (1054.9 m) |
| 9 | $2.4\ell_f$ (780.6 m) | $2.4\ell_f$ (780.6 m) |

TABLE IV. Values of the transition location ($x_t$) for BSEL and ESEL for cases 3, 5, 7, and 9.

| Case | ΔBSEL | ΔESEL |
|---|---|---|
| 3 | $2.1\ell_f$ (3472.3 m) | $1.9\ell_f$ (3141.7 m) |
| 5 | $2.1\ell_f$ (1415.4 m) | $1.8\ell_f$ (1213.2 m) |
| 7 | $2.3\ell_f$ (1011.0 m) | $2.2\ell_f$ (967.0 m) |
| 9 | $2.3\ell_f$ (748.0 m) | $2.1\ell_f$ (683.0 m) |

Similar to the N-wave procedure, hypothesis tests were conducted to determine the location of $x_t$ for the low-boom simulations. Table V presents the values of $x_t$ only for the ΔPL and ΔISBAP. For ΔDSEL, there was no clear transition region, as the p-values fell below 0.05 at nearly every location along the propagation direction. For ΔBSEL and ΔESEL, the distributions were normal only for $x_1\ell_f^{-1} < 1.0$, this was true for each rms velocity considered. Thus, the hypothesis tests show no indication of normality for ΔDSEL, while ΔBSEL and ΔESEL are only normal distributed for small values of $x_1\ell_f^{-1}$.

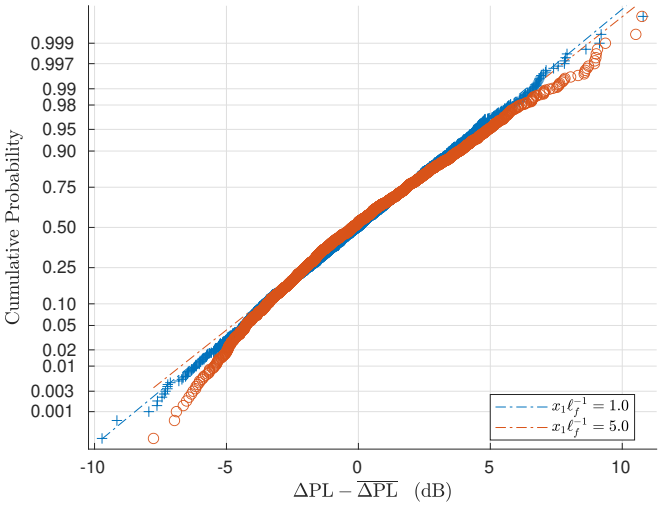


FIG. 12. Probability plot of ΔPL with respect to the average for case 9 of the low-boom simulations.

TABLE V. Values of the transition location ($x_t$) for PL and ISBAP for cases 5, 7, and 9.

| Case | ΔPL | ΔISBAP |
|---|---|---|
| 3 | $2.5\ell_f$ (4091.6 m) | N.A. |
| 5 | $2.4\ell_f$ (1729.1 m) | $4.7\ell_f$ (3386.2 m) |
| 7 | $2.5\ell_f$ (948.8 m) | $4.9\ell_f$ (1859.6 m) |
| 9 | $2.6\ell_f$ (722.4 m) | $4.7\ell_f$ (1305.9 m) |

The transition region for ΔPL is only slighlty larger on average than the N-wave results. The normality of ΔPL appears to be consistent for both waveforms considered. The values of $x_t$ for ΔISBAP were approximately twice as large as the N-wave results, a strong indication that ΔISBAP is normally distributed for longer propagation distances for the low-boom waveform than the N-wave. For case 3, hypothesis tests suggest that ΔISBAP is normally distributed in the entire domain. Although the transition region in terms of the non-dimensional distance $x_1\ell_f^{-1}$ is nearly constant for varying rms velocity, the dimensional distance, $x_1$, where $x_t$ is located decreases for both ΔPL and ΔISBAP. This result is consistent with the N-wave simulations.

### E. First and Second Moments of the Loudness Metrics

The average of the loudness metrics as a function of the normalized propagation distance provides insight into the effect of the turbulent field on the perceived loudness of both waveforms. Figure 13 shows the curves of average ΔPL, ΔISBAP, ΔBSEL, and ΔESEL for the N-wave and four separate cases. The average ΔDSEL is not shown because it overlaps with the curves for ΔBSEL, making it difficult to distinguish between the two. The average value of each metric decreases rapidly for $x_1\ell_f^{-1} \leq 2$. Beyond $x_1\ell_f^{-1} \geq 3$, the decrease is approximately linear for each turbulence condition. For the low-boom waveform (Fig. 14), each metric initially decreases rapidly along $x_1\ell_f^{-1}$. As $x_1\ell_f^{-1}$ increases, each metric approaches a constant value. The ΔESEL is not shown in Fig. 14 since it nearly overlaps the ΔISBAP results, and qualitatively there is not much to distinguish between the two. Both the N-wave and low-boom waveform were propagated a physical distance of 4094 m; however, since turbulent fields generated for the N-wave simulations did not have exactly the same value as those for the low-boom simulations (Tables I and II) the nondimensional distances propagated by each waveform were different. This is evident in the figures presented in this section, where the $x_1\ell_f^{-1}$ travelled is larger for the low-boom simulations of case 9 than it is for the N-wave simulations.

At all propagation distances, the average value of each loudness metric decreases with respect to the nominal. Bradley et al.[15] argue that this decrease is due in part to the average increase in the rise-time of the

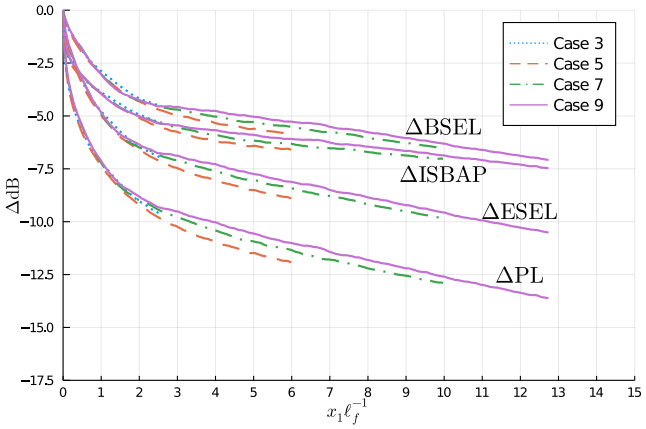


FIG. 13. Mean values of ΔPL, ΔISBAP, ΔBSEL, and ΔESEL for the N-wave.

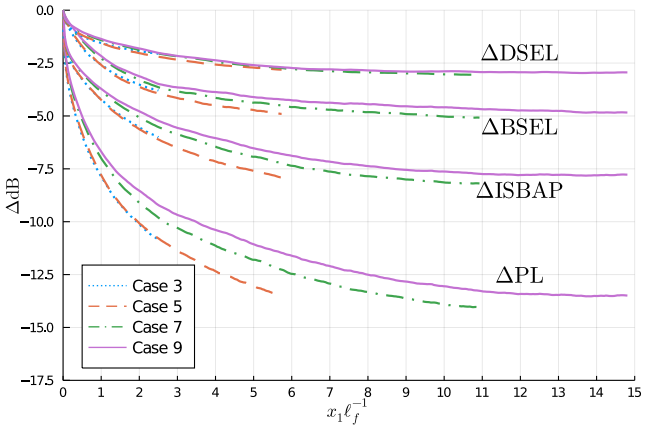


FIG. 14. Mean values of ΔPL, ΔISBAP, ΔBSEL, and ΔDSEL for the low-boom waveform.

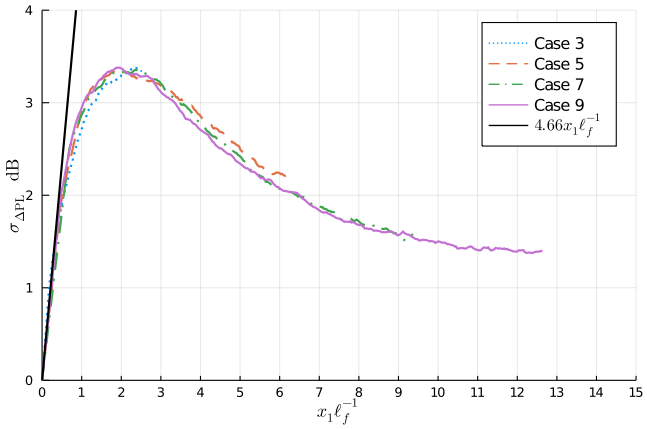


FIG. 15. Standard deviation of PL for the N-wave.

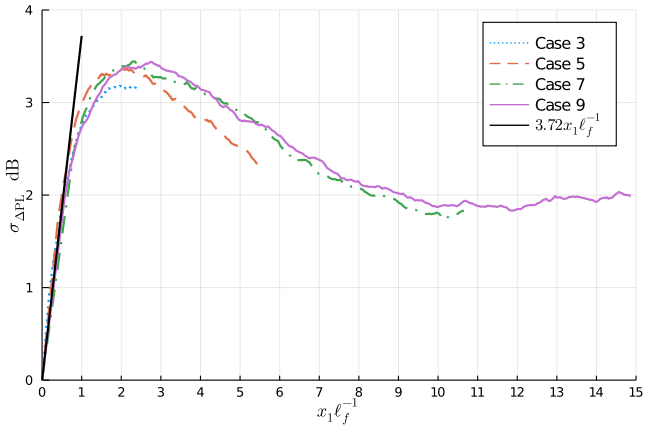


FIG. 16. Standard deviation of PL for the low-boom waveform.

wave, observed by Lipkens and Blackstock.[11] In our simulations, we also observed that the average rise time increased with propagation distance, which is consistent with the viewpoint of Bradley et al.[15] The N-wave data are well collapsed for small values of $x_1\ell_f^{-1}$; however, the low-boom data do not show a strong collapse when the propagation direction is scaled by $\ell_f$. Specifically, the propagation cases at lower turbulence intensities experience a larger drop-off in average value at the same $x_1\ell_f^{-1}$ locations for both waveforms. This is due to the sensitivity of the loudness to the rms velocity, shown in Figs. 9 and 10. In order to obtain a better collapse of the low-boom metric data, $\ell_f$ would have to be modified to account for this sensitivity.

The standard deviation of ΔPL ($\sigma_{\Delta PL}$) along the normalized propagation direction is shown in Fig. 15 for the N-wave simulations and Fig. 16 for the low-boom simulations. The $\sigma_{\Delta PL}$ of both waveforms are qualitatively very similar along $x_1\ell_f^{-1}$. The standard deviation of each metric was found to increase linearly for small values of $x_1\ell_f^{-1}$. The slope of $\sigma_{\Delta PL}$ for the N-wave in case 9 was determined to be 4.66, found by a linear regression performed for $x_1\ell_f^{-1} \leq 0.5$. For the low-boom waveform, the same process resulted in a computed slope of 3.72 for small $x_1\ell_f^{-1}$ values. For each metric considered here (ΔPL, ΔISBAP, ΔBSEL, ΔDSEL, and ΔESEL), the slope of the standard deviation at small values of $x_1\ell_f^{-1}$ is found to be consistently larger for the N-wave simulations than the low-boom simulations. This is an indication that once the N-wave begins to propagate through a layer of turbulence the variance of the loudness levels increases at a faster rate than the variance would for a shaped waveform like the one considered here. The slopes of each metric with respect to $x_1\ell_f^{-1}$ for $x_1\ell_f^{-1} \leq 0.5$ are shown in Table VI. For each metric considered, the slope of the standard deviation for the N-wave simulations is approximately 1 dB greater than the slope of the low-boom simulations.

The maximum value of the standard deviation of each metric along the propagation distance, denoted by $\sigma_{\Delta PL}^{max}$ for the ΔPL, is fairly consistent across all turbu-

TABLE VI. Numerical estimation of the rate of change of $\sigma_{\Delta\text{PL}}$, $\sigma_{\Delta\text{ISBAP}}$, $\sigma_{\Delta\text{BSEL}}$, and $\sigma_{\Delta\text{ESEL}}$ for small values of $x_1\ell_f^{-1}$.

| Metric | N-wave | Low-boom | Difference |
|---|---|---|---|
| ΔPL | 4.66 | 3.72 | 0.94 |
| ΔISBAP | 3.03 | 1.98 | 1.05 |
| ΔBSEL | 3.89 | 2.85 | 1.04 |
| ΔDSEL | 3.00 | 2.00 | 1.00 |
| ΔESEL | 4.77 | 3.73 | 1.04 |

TABLE VII. The average of the maximum values of the standard deviation of each metric across all cases, $\mu^{\sigma\max}$, and associated standard deviations, $\sigma^{\sigma\max}$.

| | N-wave | Low-boom |
|---|---|---|
| $\mu^{\sigma\max}_{\Delta\text{PL}} \pm \sigma^{\sigma\max}_{\Delta\text{PL}}$ | $3.37 \pm 0.01$ | $3.37 \pm 0.10$ |
| $\mu^{\sigma\max}_{\Delta\text{ISBAP}} \pm \sigma^{\sigma\max}_{\Delta\text{ISBAP}}$ | $3.11 \pm 0.12$ | $2.76 \pm 0.21$ |
| $\mu^{\sigma\max}_{\Delta\text{BSEL}} \pm \sigma^{\sigma\max}_{\Delta\text{BSEL}}$ | $3.14 \pm 0.03$ | $2.74 \pm 0.16$ |
| $\mu^{\sigma\max}_{\Delta\text{DSEL}} \pm \sigma^{\sigma\max}_{\Delta\text{DSEL}}$ | $2.65 \pm 0.06$ | $2.19 \pm 0.39$ |
| $\mu^{\sigma\max}_{\Delta\text{ESEL}} \pm \sigma^{\sigma\max}_{\Delta\text{ESEL}}$ | $3.26 \pm 0.02$ | $2.87 \pm 0.12$ |

lence rms velocities. Since these values are close in magnitude for each turbulence case, we will examine the average and standard deviation of $\sigma^{\max}_{\Delta\text{PL}}$, $\sigma^{\max}_{\Delta\text{ISBAP}}$, $\sigma^{\max}_{\Delta\text{BSEL}}$, $\sigma^{\max}_{\Delta\text{DSEL}}$, and $\sigma^{\max}_{\Delta\text{ESEL}}$ computed from all cases. The average value will be denoted $\mu^{\sigma\max}_{\Delta\text{PL}}$ for the PL and the standard deviation is $\sigma^{\sigma\max}_{\Delta\text{PL}}$. Table VII shows values of $\mu^{\sigma\max} \pm \sigma^{\sigma\max}$ for all metrics of the N-wave and low-boom simulations. The deviation of $\sigma^{\max}$ is small for the N-wave simulations. This indicates that the magnitude of the maximum standard deviation of each metric attained in the N-wave simulations is independent of the turbulence rms velocity. Additionally, the location where the standard deviation attains a maximum for the N-wave cases is generally well collapsed across different rms velocities. For the ΔPL, this location is approximately $x_1\ell_f^{-1} = 2$. For the low-boom simulations, the deviation of $\sigma^{\max}$ is larger than the N-wave simulations. However, the $\sigma^{\sigma\max}$ values are still less than 10% of the $\mu^{\sigma\max}$ values for all but the ΔDSEL, indicating that the spread of $\sigma^{\max}$ is small for the low-boom simulations as well. The $\mu^{\sigma\max}$ values of the metrics for the N-wave simulations are always larger than those for the low-boom, except for ΔPL, which matches up to three significant figures. From this, we can infer that the variation in loudness is larger on average for the N-wave than the low-boom waveform.

## V. SUMMARY AND CONCLUSIONS

The effects of a kinematic field of turbulence on the loudness metrics for an N-wave and the low-boom waveform of the NASA X-59 QueSST were investigated numerically with a one-way propagation method. The two waveforms are not greatly affected by nonlinearity. A length scale, $\ell_f$, was proposed to account for the effect of the rms velocity and turbulence integral scale on the formation of caustics. Across the range of $u_{\text{rms}}$ values considered, the PDF of $x_{\text{caust}}$ attains a maximum around $x_1\ell_f^{-1} = 1$. The mean values of ΔPL, ΔISBAP, ΔBSEL, ΔDSEL, and ΔESEL collapse for the N-wave in the range $x_1\ell_f^{-1} \leq 2$. For shaped waveforms, scaling the propagation distance in terms of $\ell_f$ is not adequate to collapse the mean loudness metric data, which at the same $x_1\ell_f^{-1}$ locations varies with rms velocity of the turbulence. However, the standard deviation of ΔPL for the shaped waveform is more consistent with some of the features observed in the N-wave data; and shows a collapse of the data for high rms velocities. For the N-wave, the agreement of $\sigma_{\Delta\text{PL}}$ across several different cases hints at the potential to model $\sigma_{\Delta\text{PL}}$ by a function of the nondimensional distance. Researchers who desire a quick estimation of the variance of PL would find such a function useful.

The loudness decreases along the propagation direction for both waveforms. Most of the decrease in the loudness levels occurs in the range 100 Hz to 1000 Hz. The loudness levels at fixed $x_1\ell_f^{-1}$ locations show some sensitivity to the $u_{\text{rms}}$ value. When the $u_{\text{rms}}$ increases at these fixed locations, the loudness increases slightly. For $x_1\ell_f^{-1} = 1$, frequencies between 355-560 Hz are the most sensitive to changes in $u_{\text{rms}}$, and as $x_1\ell_f^{-1}$ increases the loudness at lower frequencies become more sensitive to changes in the rms velocity. In the future, any improvements to $\ell_f$ would have to reduce the sensitivity in the range of 100 Hz to 1000 Hz.

The distributions of ΔPL, ΔISBAP, ΔBSEL, and ΔESEL are initially normal as the sonic boom propagates through turbulence. Plots of the cumulative probability, along with hypothesis testing, indicate that the ΔPL begins to deviate from a normal distribution as it propagates through turbulence. The hypothesis tests for the N-wave simulations suggest that the location where ΔPL, ΔISBAP, ΔBSEL, and ΔESEL transition from being normally distributed to skewed right of the normal distribution is in the range $1.8 \leq x_1\ell_f^{-1} \leq 2.5$. This is also the range where the standard deviation of ΔPL, ΔISBAP, ΔBSEL, and ΔESEL reach a maximum value. In terms of physical distance, the transition location for the N-wave simulations decreases as the rms velocity increases. When considering the low-boom simulations, the transition locations for ΔPL are only slightly larger than the N-wave results. For the ΔISBAP, the transition locations are approximately twice as large as the N-wave results, indicating that the distributions remain normal for longer propagation distances than the N-wave. The simulations performed here suggest that the ΔPL and

ΔISBAP for both waveforms, while initially normally distributed in the turbulent field, will not remain normally distributed indefinitely as the sonic boom continues to propagate through a turbulent field. There is also evidence from the hypothesis testing that the proposed scaling length, $\ell_f$, is able to parameterize the location where the loudness metrics are no longer normally distributed. This location falls in the range $1.8\ell_f \leq x_t \leq 2.6\ell_f$ for the N-wave loudness metrics and the low-boom ΔPL, and $4.7\ell_f \leq x_t \leq 4.9\ell_f$ for the low-boom ΔISBAP.

The loudness metrics that correlate well with annoyance (PL, ISBAP, BSEL, DSEL, and ESEL) all have mean values that decrease along the propagation direction. When scaled by $\ell_f$, the curves of each metric along the propagation direction are similar. The isotropic turbulence field has a similar effect on the metrics across a wide range of rms velocities for both waveforms. The standard deviation of each metric considered here is directly proportional to $x_1\ell_f^{-1}$ for small values of $x_1\ell_f^{-1}$. The maximum value attained by the standard deviation of each metric in the simulations is independent of the rms velocity of the turbulence for both the N-wave and low-boom. This implies that for a real sonic boom propagating in the atmospheric boundary layer region, the maximum variation in the loudness that is possible is dependent on the distance the waveform propagates through the turbulence. For lower turbulence rms velocities, the propagation distance required to reach the location of maximum loudness variation is larger than the distance required for higher turbulence rms velocities. In all of the simulations, the standard deviation of ΔPL reaches a maximum value in the range $1 \leq x_1\ell_f^{-1} \leq 3$. Therefore, one can infer that sonic boom signals recorded on the ground in regions where the propagation distance through the ABL is between $\ell_f^{-1}$ and $3\ell_f^{-1}$ are likely to have the highest variability in the PL metric, compared to other regions of the sonic boom carpet.

## ACKNOWLEDGMENTS

This material is based upon work supported by the Commercial Supersonic Technology Project of the National Aeronautics and Space Administration under Grant No. 80NSSC19K1685 issued through the NASA Fellowship Activity.

[1]D. J. Maglieri, P. J. Bobbitt, K. J. Plotkin, K. P. Shepherd, P. G. Coen, and D. M. Richwine, "Sonic boom: Six decades of research," NASA/SP-2014-622, NASA Langley Research Center, Hampton, Virginia (2014).

[2]D. Hilton, V. Huckel, and D. Maglieri, "Sonic boom measurements during bomber training operation in the chicago area," NASA TN-D2655, Langley Research Center (1966).

[3]A. D. Pierce and D. J. Maglieri, "Effects of atmospheric irregularities on sonic-boom propagation," The Journal of the Acoustical Society of America **51**(2C), 702–721 (1972) https://doi.org/10.1121/1.1912904 doi: 10.1121/1.1912904.

[4]M. P. Friedman, E. J. Kane, and A. Sigalla, "Effects of atmosphere and aircraft motion on the location and intensity of a sonic boom," AIAA Journal **1**(6), 1327–1335 (1963) https://doi.org/10.2514/3.1788 doi: 10.2514/3.1788.

[5]W. D. Hayes and H. L. Runyan, "Sonic-boom propagation through a stratified atmosphere," The Journal of the Acoustical Society of America **51**(2C), 695–701 (1972) https://doi.org/10.1121/1.1912903 doi: 10.1121/1.1912903.

[6]C. L. Thomas, "Extrapolation of sonic boom pressure signatures by the waveform parameter method," NASA-TN-D-6832, Ames Research Center, Moffet Field, California (1972).

[7]K. J. Plotkin, M. Downing, and J. Page, "USAF single event sonic boom prediction model: PCBOOM," The Journal of the Acoustical Society of America **95**(5), 2839–2839 (1994) https://doi.org/10.1121/1.409605 doi: 10.1121/1.409605.

[8]P. V. Yuldashev, S. Ollivier, M. M. Karzova, V. A. Khokhlova, and P. Blanc-Benon, "Statistics of peak overpressure and shock steepness for linear and nonlinear N-wave propagation in a kinematic turbulence," The Journal of the Acoustical Society of America **142**(6), 3402–3415 (2017) https://doi.org/10.1121/1.5015991 doi: 10.1121/1.5015991.

[9]T. Stout, "Simulation of N-wave and shaped supersonic signature turbulent variations," Ph.D. thesis, Pennsylvania State University, 2018.

[10]D. Luquet, "3D simulation of acoustical shock waves propagation through a turbulent atmosphere. Application to sonic boom," Theses, Université Pierre et Marie Curie - Paris VI, 2016, https://tel.archives-ouvertes.fr/tel-01360574.

[11]B. Lipkens and D. T. Blackstock, "Model experiment to study sonic boom propagation through turbulence. Part I: General results," The Journal of the Acoustical Society of America **103**(1), 148–158 (1998) doi: 10.1121/1.421114.

[12]M. Averiyanov, S. Ollivier, V. Khokhlova, and P. Blanc-Benon, "Random focusing of nonlinear acoustic N-waves in fully developed turbulence: Laboratory scale experiment," The Journal of the Acoustical Society of America **130**(6), 3595–3607 (2011) https://doi.org/10.1121/1.3652869 doi: 10.1121/1.3652869.

[13]S. S. Stevens, "Perceived level of noise by Mark VII and decibels (E)," The Journal of the Acoustical Society of America **51**(2B), 575–601 (1972) https://doi.org/10.1121/1.1912880 doi: 10.1121/1.1912880.

[14]A. Loubeau, S. R. Wilson, and J. Rathsam, "Updated evaluation of sonic boom noise metrics," The Journal of the Acoustical Society of America **144**(3), 1706–1706 (2018) https://doi.org/10.1121/1.5067578 doi: 10.1121/1.5067578.

[15]K. A. Bradley, C. M. Hobbs, C. B. Wilmer, V. W. Sparrow, T. A. Stout, J. M. Morgenstern, K. H. Underwood, D. J. Maglieri, R. A. Cowart, M. T. Collmar, H. Shen, and P. Blanc-Benon, "Sonic booms in atmospheric turbulence (SonicBAT): The influence of turbulence on shaped sonic booms," NASA Technical Report (2020).

[16]B. A. Davy and D. T. Blackstock, "Measurements of the refraction and diffraction of a short N wave by a gas-filled soap bubble," The Journal of the Acoustical Society of America **49**(3B), 732–737 (1971) https://doi.org/10.1121/1.1912410 doi: 10.1121/1.1912410.

[17]A. D. Pierce, "Spikes on sonic-boom pressure waveforms," The Journal of the Acoustical Society of America **44**(4), 1052–1061 (1968) https://doi.org/10.1121/1.1911195 doi: 10.1121/1.1911195.

[18]H. S. Ribner, P. J. Morris, and W. H. Chu, "Laboratory simulation of development of superbooms by atmospheric turbulence," The Journal of the Acoustical Society of America **53**(3), 926–928 (1973) https://doi.org/10.1121/1.1913411 doi: 10.1121/1.1913411.

[19]S. Ollivier and P. Blanc-Benon, "Model experiments to study acoustic n-wave propagation through turbulent media," in *10th AIAA/CEAS Aeroacoustics Conference*, American Institute of Aeronautics and Astronautics (2004), https://doi.org/10.2514/6.2004-2921, doi: 10.2514/6.2004-2921.

[20]F. Dagrau, M. Rénier, R. Marchiano, and F. Coulouvrat, "Acoustic shock wave propagation in a heterogeneous medium: A numerical simulation beyond the parabolic approximation," The Journal of the Acoustical Society of America **130**(1), 20–32 (2011) https://doi.org/10.1121/1.3583549 doi: 10.1121/1.3583549.

[21]R. V. Khokhlov, K. A. Naugol'nykh, and S. I. Soluyan, "Waves of moderate amplitudes in absorbing media," Acustica **14**(5), 248–253 (1964).

[22]E. A. Zabolotskaya and R. V. Khokhlov, "Quasi-plane waves in the nonlinear acoustics of confined beams," Sov. Phys. Acoust. **15**, 35–40 (1969).

[23]R. Leconte, R. Marchiano, J.-C. Chassaing, and F. Coulouvrat, "Sensitivity of sonic boom propagation throughout a turbulent atmosphere," The Journal of the Acoustical Society of America **146**(4), 2782–2782 (2019) https://doi.org/10.1121/1.5136635 doi: 10.1121/1.5136635.

[24]R. Leconte, R. Marchiano, F. Coulouvrat, and J.-C. Chassaing, "Influence of atmospheric turbulence parameters on the propagation of sonic boom," (2020) https://hal.archives-ouvertes.fr/FA2020/hal-03229477 doi: 10.48465/FA.2020.0329.

[25]R. Leconte, J.-C. Chassaing, F. Coulouvrat, and R. Marchiano, "Simulation of the propagation of classical and low booms through turbulent wind fluctuations," The Journal of the Acoustical Society of America **149**(4), A73–A73 (2021) https://doi.org/10.1121/10.0004556 doi: 10.1121/10.0004556.

[26]P. Blanc-Benon, L. Dallois, and D. Juvé, "Long range sound propagation in a turbulent atmosphere within the parabolic approximation," Acta Acustica united with Acustica **87**, 659–669 (2001).

[27]L. L. Locey and V. W. Sparrow, "Modeling atmospheric turbulence as a filter for sonic boom propagation," Noise Control Engineering Journal **55**(6), 495–503 (2007) https://doi.org/10.3397/1.2817810 doi: 10.3397/1.2817810.

[28]T. A. Stout, V. W. Sparrow, and P. Blanc-Benon, "Evaluation of numerical predictions of sonic boom level variability due to atmospheric turbulence," The Journal of the Acoustical Society of America **149**(5), 3250–3260 (2021) https://doi.org/10.1121/10.0004985 doi: 10.1121/10.0004985.

[29]F. Coulouvrat, "New equations for nonlinear acoustics in a low mach number and weakly heterogeneous atmosphere," Wave Motion **49**(1), 50–63 (2012) https://doi.org/10.1016/j.wavemoti.2011.07.002 doi: 10.1016/j.wavemoti.2011.07.002.

[30]M. J. Lighthill, *Waves in fluids* (Cambridge University Press, Cambridge England New York, 1978).

[31]G. K. Batchelor, *The theory of homogeneous turbulence* (Cambridge University Press, Cambridge New York, 1982).

[32]G. Strang, "On the construction and comparison of difference schemes," SIAM Journal on Numerical Analysis **5**(3), 506–517 (1968) https://doi.org/10.1137/0705041 doi: 10.1137/0705041.

[33]J. Goodman, *Introduction to Fourier optics* (Roberts & Co, Englewood, Colo, 2005).

[34]L. Ganjehi, R. Marchiano, F. Coulouvrat, and J.-L. Thomas, "Evidence of wave front folding of sonic booms by a laboratory-scale deterministic experiment of shock waves in a heterogeneous medium," The Journal of the Acoustical Society of America **124**(1), 57–71 (2008) https://doi.org/10.1121/1.2832621 doi: 10.1121/1.2832621.

[35]J. Crank and P. Nicolson, "A practical method for numerical evaluation of solutions of partial differential equations of the heat-conduction type," Mathematical Proceedings of the Cambridge Philosophical Society **43**(1), 50–67 (1947) https://doi.org/10.1017/s0305004100023197 doi: 10.1017/s0305004100023197.

[36]W. D. Hayes, R. C. Haefeli, and H. E. Kulsrud, "Sonic boom propagation in a stratified atmosphere, with a computer program," NASA CR-1299, National Aeronautics and Space Administration (1969).

[37]F. Coulouvrat, "A quasi-analytical shock solution for general nonlinear progressive waves," Wave Motion **46**(2), 97–107 (2009) https://doi.org/10.1016/j.wavemoti.2008.09.002 doi: 10.1016/j.wavemoti.2008.09.002.

[38]W. M. Spurlock, M. J. Aftosmis, and M. Nemec, "Cartesian mesh simulations for the third AIAA sonic boom prediction workshop," in *AIAA Scitech 2021 Forum*, American Institute of Aeronautics and Astronautics (2021), https://doi.org/10.2514/6.2021-0473, doi: 10.2514/6.2021-0473.

[39]J. B. Lonzaga, "Recent enhancements to NASA's PCBoom sonic boom propagation code," in *AIAA Aviation 2019 Forum*, American Institute of Aeronautics and Astronautics (2019), https://doi.org/10.2514/6.2019-3386, doi: 10.2514/6.2019-3386.

[40]J. A. Page, J. B. Lonzaga, M. J. Shumway, S. R. Kaye, R. S. Downs, A. Loubeau, and W. J. Doebler, "PCBoom version 7.1 user's guide," NASA TM 20205007703, Langley Research Center (2020).

[41]C. Klipp, "Turbulence anisotropy in the near-surface atmosphere and the evaluation of multiple outer length scales," Boundary-Layer Meteorology **151**(1), 57–77 (2013) https://doi.org/10.1007/s10546-013-9884-0 doi: 10.1007/s10546-013-9884-0.

[42]R. Frehlich, L. Cornman, and R. Sharman, "Simulation of three-dimensional turbulent velocity fields," Journal of Applied Meteorology **40**(2), 246–258 (2001) https://doi.org/10.1175/1520-0450(2001)040<0246:sotdtv>2.0.co;2 doi: 10.1175/1520-0450(2001)040<0246:sotdtv>2.0.co;2.

[43]A. S. Monin and A. M. Yaglom, *Statistical fluid mechanics : mechanics of turbulence* (Dover Publications, Inc, Mineola, New York, 2007).

[44]T. von Karman, "Progress in the statistical theory of turbulence," Proceedings of the National Academy of Sciences **34**(11), 530–539 (1948) https://doi.org/10.1073/pnas.34.11.530 doi: 10.1073/pnas.34.11.530.

[45]D. K. Wilson, "A three-dimensional correlation/spectral model for turbulent velocities in a convective boundary layer," Boundary-Layer Meteorology **85**(1), 35–52 (1997) https://doi.org/10.1023/a:1000418709945 doi: 10.1023/a:1000418709945.

[46]M. Shinozuka, "Simulation of multivariate and multidimensional random processes," The Journal of the Acoustical Society of America **49**(1B), 357–368 (1971) https://doi.org/10.1121/1.1912338 doi: 10.1121/1.1912338.

[47]D. K. Wilson, "Three-dimensional correlation and spectral functions for turbulent velocities in homogeneous and surface-blocked boundary layers.," Army Research Laboratory (1997), https://doi.org/10.21236/ada327709, doi: 10.21236/ada327709.

[48]V. E. Ostashev and D. K. Wilson, *Acoustics in moving inhomogeneous media* (CRC Press, Taylor & Francis Group, Boca Raton, FL, 2016).

[49]V. A. Kulkarny and B. S. White, "Focusing of waves in turbulent inhomogeneous media," Physics of Fluids **25**(10), 1770–1784 (1982) https://doi.org/10.1063/1.863654 doi: 10.1063/1.863654.

[50]P. Blanc-Benon, D. Juvè, and G. Comte-Bellot, "Occurrence of caustics for high-frequency acoustic waves propagating through turbulent fields," Theoretical and Computational Fluid Dynamics **2**(5-6), 271–278 (1991) https://doi.org/10.1007/bf00271467 doi: 10.1007/bf00271467.

[51]O. Rudenko and B. Enflo, "Nonlinear N-wave propagation through a one-dimensional phase screen," Acta Acustica united with Acustica **86**(2), 229–238 (2000).

[52]G. Jackson and H. Leventhall, "Calculation of the perceived level of noise (PLdB) using Stevens' method (Mark VII)," Applied Acoustics **6**(1), 23–34 (1973) https://doi.org/10.1016/0003-682x(73)90027-3 doi: 10.1016/0003-682x(73)90027-3.

[53]T. W. Anderson and D. A. Darling, "A test of goodness of fit," Journal of the American Statistical Association **49**(268), 765–769 (1954) https://www.tandfonline.com/doi/abs/10.1080/01621459.1954.10501232 doi: 10.1080/01621459.1954.10501232.

[54]A. N. Kolmogorov, "Sulla determinazione empirica di una legge di distribuzione," G. Ist. Ital. Attuari 83–91 (1933).

[55]R. L. Wasserstein and N. A. Lazar, "The ASA statement on p-values: context, process, and purpose," The American Statistician **70**(2), 129–133 (2016) https://doi.org/10.1080/00031305.2016.1154108 doi: 10.1080/00031305.2016.1154108.